NUCL SCI TECH (2020) 31:68
https://doi.org/10.1007/s41365-020-00774-x

Lattice design for a hybrid multi-bend achromat light source

Eun-San Kim[1]

Received: 25 January 2020 / Revised: 13 April 2020 / Accepted: 6 May 2020 / Published online: 20 June 2020

Abstract We present a lattice design and beam dynamics analysis for a 4 GeV low-emittance, high-brilliance synchrotron light source. The lattice consisted of 26 six-bend achromats with 26 long and 26 short straight sections. We present the design results for a hybrid multi-bend achromat (HMBA) lattice with a natural emittance of 168 pm and circumference of 729.3 m. Each cell had 4 longitudinal gradient bendings, 2 combined bendings, 14 quadrupoles, and 2 families of sextupoles. The lattice was designed to be flexible to provide both nonzero and zero dispersion functions in the long straight section. The two straight sections in each cell had lengths of 5.6 and 1.2 m. To ensure sufficient injection, we optimized the design lattice and dynamic aperture. We investigated the dynamic aperture in the lattice with machine errors, and the results showed that the lattice design provides sufficient dynamic aperture after COD correction for beam injection. We present the results of an injection scheme that demonstrates the space in the injection section and the particle motions of the injected beam. We also present the results of beam tracking after the beam injection to examine the characteristics of the beam injection. The designed HMBA lattice was well optimized in terms of the beam parameters and brilliance as an intermediate light source at 4 GeV and a circumference of 729.3 m.

This work was supported by NRF-2019R1A2C1089393.

✉ Eun-San Kim
eskim1@korea.ac.kr

1 Department of Accelerator Science, Korea University Sejong Campus, Sejong 30019, Korea

Keywords Hybrid multi-bend achromat · Dynamic aperture · Beam injection · Beam tracking

1 Introduction

Significant progress has been made in the development of low-emittance light sources over the last two decades. Double-bend-achromat (DBA) and triple-bend-achromat (TBA) lattices have been adopted by most third-generation light sources. Moreover, the user requirements for low-emittance storage rings have become increasingly demanding. In response, there have been many improvements in the design and operation of the light sources [1–14]. Users require a number of undulator beamlines with both high-flux and high-brightness photons, ranging from soft to hard X-rays.

Several low-emittance light sources in the energy range of 3–6 GeV have been developed to provide high brilliance in the hard X-ray range. The 3 GeV MAX-IV storage ring initiated a new trend of lattice design that adopted a multi-bend achromat (MBA) lattice to obtain a low-emittance beam [15]. In comparison with existing storage rings, this provides significantly brighter X-ray photons in the energy range of 1–30 keV. The MBA lattices focus on the dispersion function by locating high-gradient quadrupoles between vertical-focusing dipoles. This method is effective in decreasing natural emittance. The dispersion function in the MBA lattice is reduced to low values that result in a reduction in beam emittance.

Recently, many research and development efforts have been made toward upgrading the performances of existing third-generation light sources using facilities such as the advanced photon source (APS) and European synchrotron radiation facility (ESRF) [16, 17]. They adopted a hybrid MBA (HMBA) method to decrease the emittance that was initially applied in the 6 GeV ESRF extremely brilliant source (ESRF-EBS). The natural emittance in an HMBA lattice can be reduced by more than two orders of magnitude compared to that of DBA and TBA lattices. The use of combined-function dipole magnets and longitudinal-gradient dipole magnets redistributes the bending and focusing functions inside the cell to achieve lower emittance. The middle bending magnets in the HMBA are often combined-function magnets, which also act as defocusing quadrupoles. This efficiently uses the space and reduces the emittance by increasing the horizontal damping partition number. Dipole magnets with varying longitudinal-gradient fields are utilized to further reduce the beam emittance.

The various requirements of the next low-emittance domestic light source are as follows: circumference less than 800 m, beam energy of around 4 GeV, and brilliance of the order of 10^{22} on undulators. Thus, we designed a lattice that satisfies these requirements and demonstrated the results. Thus, one of the motivations for this paper is to present the design results for an HMBA lattice with an emittance of 168 pm in a 4 GeV ring with 26 cells and a circumference of 729.3 m. With the short straight sections in the normal cells, the number of beamlines is doubled. The lattice is designed to provide both achromatic and non-achromatic HMBA lattices. Therefore, we demonstrate the characteristics and performance of a 4 GeV HMBA storage ring with an additional short straight section.

Because a low-emittance lattice is affected by the nonlinear beam dynamics in the ring, it is necessary to achieve an adequate dynamic aperture, which may affect beam injection and lifetime. We investigated the effects of magnet misalignments on the dynamic aperture. A correction of the closed orbit distortion (COD) was performed in the designed lattice, which showed that the lattice provided a sufficient dynamic aperture. As a result, we selected an optimal tune for the lattice.

The injection section in the ring consisted of one septum magnet and four kicker magnets. The beam was injected into the ring horizontally using the off-axis injection method. We displayed the simulation results on beam tracking for the beam injection. We used the computer code Strategic accelerator design (SAD) for the lattice design, dynamic aperture, and beam injection [18].

In Sect. 2, we present the designs for the 4 GeV HMBA lattice. Section 3 provides the results of COD correction and the effects of machine errors on the dynamic aperture in the ring. Section 4 shows the tracking simulation results for beam injection. This is followed by the conclusion.

2 Lattice design for HMBA

A DBA lattice provides a large dispersion bump in the region where the sextupoles are installed. The required strength of the sextupoles can be reduced due to the large dispersion function and a large dynamic aperture can be achieved. The emittance can be further reduced through the combination of an MBA lattice and combined-function magnets. The strongly focused optics results in large chromaticity and a small dispersion function. The required strengths of the chromatic sextupoles become strong, and the dynamic aperture becomes small.

The natural emittance is expressed as $\epsilon_x\,(\mathrm{m}\cdot\mathrm{rad}) = C_qF\gamma^2\,\theta^3/J_x12\sqrt{15}$, where the Compton wavelength of the electron $C_q = 3.83\times10^{-13}$ m, γ is the Lorentz energy factor, θ is the bending angle per cell, J_x is the horizontal damping partition, and F is a form factor. The HMBA lattice consists of a combined MBA-like structure and two DBA-like structures that provide large dispersion functions. To prohibit the degradation of the natural emittance, the bending magnets on the dispersion bumps include longitudinal gradients. As the dispersion function increases, the magnetic field should be reduced. At present, ESRF-EBS and APS Upgrade (APS-U) have adopted this type of lattice.

Our lattice design consisted of 26 cells with an HMBA structure. Each cell included 4 longitudinal-gradient dipoles (2×B1, $2\times B2$), 14 quadrupoles ($2\times Q1$, $2\times Q2$, $2\times Q3$, $2\times Q4$, $2\times Q5$, $2\times Q6$, and $2\times Q7$), and 6 sextupoles ($2\times SF$, $4\times SD$). The maximum strength in the quadrupoles was 70 T/m. The B1, B2, Q1, Q2, Q3, Q4, Q5, Q6, Q7, SD, and SF magnets could be connected in series to a single power supply. The short straight section was inserted in the center section of the HMBA lattice. Thus, each cell included two straight sections with lengths of 5.6

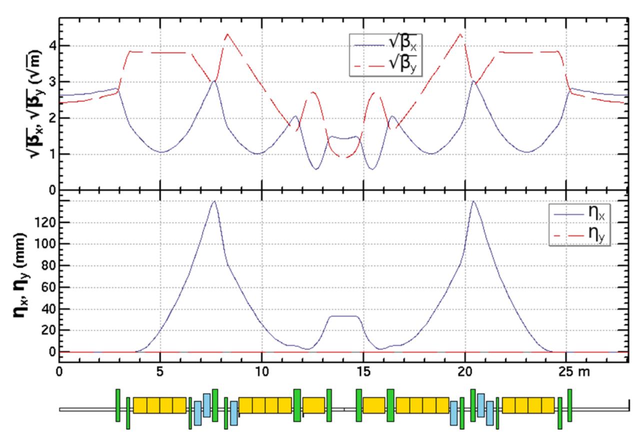

Fig. 1 (Color online) A cell in the achromatic lattice with an emittance of 168 pm (upper). One cell consists of 2 combined-bending magnets (yellow), 4 longitudinal-gradient bending magnets (striped yellow), 14 quadrupole magnets (green), and 6 sextupole magnets (blue) (lower)

and 1.2 m. Figure 1(upper) shows the lattice of one cell with an emittance of 168 pm, which has a nonzero dispersion in the long straight section. Figure 1(lower) shows the lattice of one cell that has zero dispersion in the long straight section. Control of the dispersion function could practically be performed without affecting the betatron function. Additionally, the beta functions in the straight sections could be adjusted in this lattice for various operation modes. Table 1 shows the main parameters for the proposed designed lattice. Here, x and y denote the horizontal and vertical directions, respectively.

Figure 2 shows the value of the $H_x = \gamma\eta_x^2 + 2\alpha_x\eta_x\eta_{px} + \beta_x\eta_{px}^2$ function, which is sufficiently large to obtain a large dispersion function in the DBA section for chromatic correction. Each DBA section can create a large dispersion bump for chromatic correction. The dipole field is stronger in the combined-function magnets located at both sides of the short straight section. Thus, the dipole field is stronger in the region of low H function. Vertical focusing was performed by four longitudinal gradient dipoles in a cell; each dipole has a length of 2.58 m and 4 different types of bending degrees, with a maximum magnetic field of 0.33 T. There are 2 combined-function dipoles in a cell, each with a length of 1.09 m, bending degree of 2.23°, gradient of 26.3T/m, and magnetic field of 0.48 T.

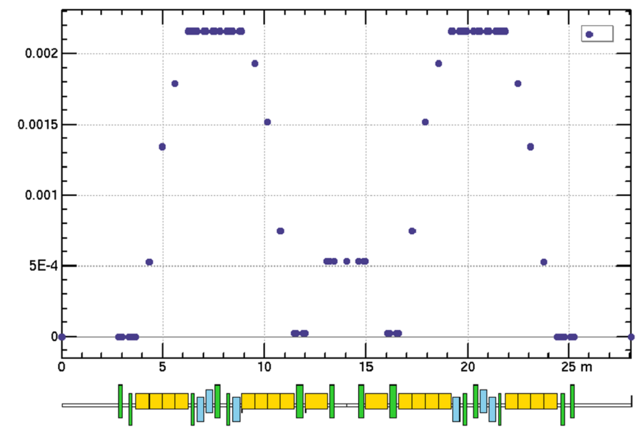

Fig. 2 (Color online) The value of $H_x = \gamma\eta_x^2 + 2\alpha_x\eta_x\eta_{px} + \beta_x\eta_{px}^2$ in one cell

A low-emittance lattice results in large natural chromaticities, which need to be compensated by sextupoles in the ring. The nonlinear effects due to the strong sextupoles

Table 1 Main parameters for the designed ring

Parameters	Value
Lattice type	HMBA
Beam energy (GeV)	4
Natural beam emittance (pm)	168
Structure	achromat
Circumference (m)	729.3
Magnetic field in combined dipole (T)	0.48
Gradient in combined dipole (T/m)	− 26.3
RF frequency (MHz)	500
Harmonic number	1216
Number of cells	26
RMS energy spread	6.68×10^{-4}
Beam size (x, y) at long straight section (μm)	34/31
Momentum compaction factor	1.04×10^{-4}
RF bucket height (%)	4.1
Energy loss per turn (MeV)	0.560
Touschek lifetime (h) at 400 mA and 1% coupling	3
Damping time (x/y/z) (ms)	24.2/34.7/22.1
Damping partition number (x/y/z)	1.43/1/1.56
RMS bunch length (mm)	2.56
RF voltage (MV)	2.5
Natural chromaticity (x/y)	− 80.25/− 70.32
Corrected chromaticity	0.1/0.1
Maximum strength of sextupole (T/m^2)	1709
Betatron tune (x/y)	59.26/20.54
Beta function (x/y) in long straight section (m)	7/6
Dispersion function (x)—in long/short straight section (m)	0.0/0.033

can reduce the dynamic aperture if they are not also adequately compensated. Therefore, we need to achieve a size of dynamic aperture sufficient for efficient beam injection and appropriate lifetime. In our lattice, the nonlinear effects of the sextupoles were reduced by a horizontal phase advance with approximately half an integer between the sextupole locations in the cell. Compensation of the chromaticity can be executed effectively when the dispersion function and beta function are large at the locations of the sextupoles. There were three sextupoles in each dispersion bump; thus, six sextupoles per cell were employed for nonlinear optimization. To decrease the strength of the sextupoles, we installed them in positions where the dispersion function had large values. We designed the lattice to have two families of sextupoles: one focusing and one defocusing, each with a length of 32.5 cm. To compensate for the chromaticity, the required sextupole strengths were $K_2 = (-1177, 1709)$ /m^3, where K_2 is defined by $\frac{dB_y}{B\rho dx^2}$. To achieve a large dynamic aperture, we investigated the optimal locations and strengths of the sextupoles, betatron tune, dispersion function, and separation of horizontal and vertical betatron functions.

To generate hard X-rays in the undulator at a beam energy of 4 GeV, the undulator period was reduced to approximately 2 cm. The thickness of the permanent magnet for the undulator pole was 5 mm. To form a sinusoidal magnetic field on the beam axis, the gap between the undulator poles needed to be of the same dimension as the pole thickness. Figure 3 shows the brilliance for undulators of 4 and 0.8 m in the long straight and short straight sections, respectively, with a total beam current of 400 mA. The in-vacuum undulator had the following parameters: a period of 22 mm, a gap of 8 mm, and a K-value of 1.52. The brightness at the long straight section amounted to 10^{22} at 10 keV. With the strongly focused lattice, the brightness for the short undulator, of length 0.8 m, was approximately 10^{21}, which is comparable to the maximum brightness of the most recent third-generation light sources.

Figure 4 shows the brilliance for the combined-bending magnet of 0.48 T with a total beam current of 400 mA. It shows a brightness close to 10^{18} around 10 keV. Figure 5 shows the Touschek beam lifetime as a function of momentum acceptance for the different numbers of bunches in the 400 mA beam current. The Touschek beam lifetime was approximately 3 h with a momentum acceptance of 3.5% in a coupling constant of 1%. Growth of the emittance due to intrabeam scattering can also be suppressed with bunch lengthening by the third harmonic cavity. Figure 6 shows the bunch lengthening, energy spread, and beam emittance for different numbers of bunches in the beam current of 400 mA due to intrabeam scattering. Here, the RF voltage is 2.5 MV and the coupling constant is 1%.

Figure 7 shows the variations in the horizontal and vertical betatron tunes in the long straight section as a function of particle momentum. Figure 8 shows the horizontal and vertical tune shifts as a function of amplitude in the horizontal and vertical planes, respectively. Here, the horizontal and vertical amplitudes were normalized to their beam sizes. This demonstrates that horizontal and vertical amplitudes with $200\sigma_x$ and $240\sigma_y$ survive in the horizontal and vertical phase spaces, respectively. Figure 9 shows the variations in the horizontal and vertical betatron functions in the long straight section as a function of particle momentum.

We performed particle tracking to examine the nonlinear effects of particles. Figure 10 shows the particle motions in phase space with normalized scales for the on-momentum particles in the lattice. The intervals of the

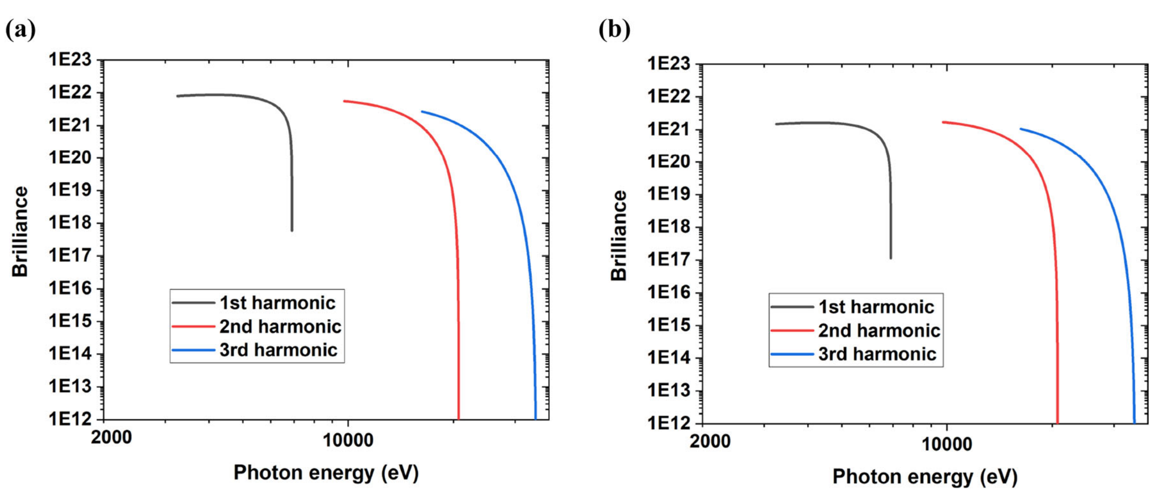

Fig. 3 (Color online) Brilliances (photons/s/mm^2/mrad^2/0.1%BW) in **a** the long straight section and **b** the short straight section

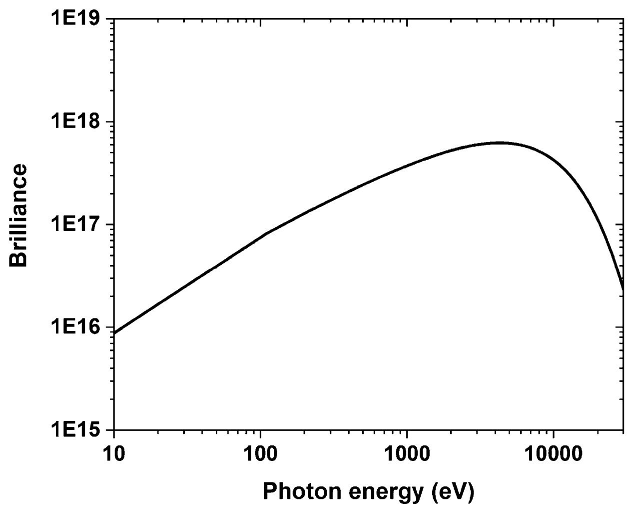

Fig. 4 Brilliance (photons/s/mm^2/mrad^2/0.1%BW) in the combined-bending magnet with 0.48 T

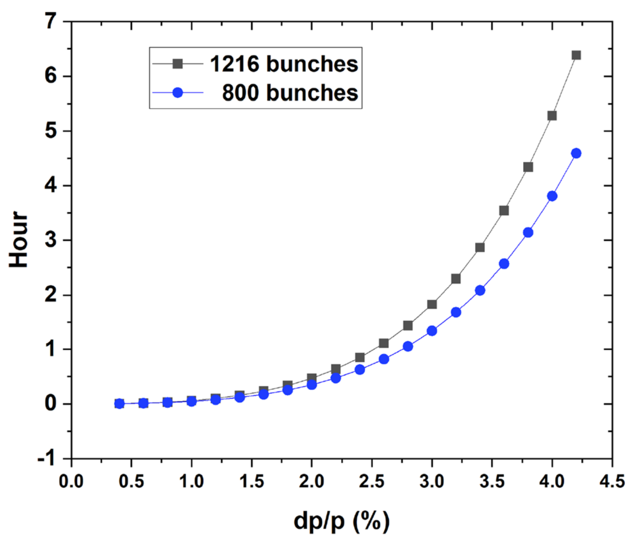

Fig. 5 Beam lifetime versus momentum acceptance for a beam current of 400 mA

initial coordinates of the plotted particles in phase space were $20\sigma_x$ and $20\sigma_y$, starting from $1\sigma_x$ and $1\sigma_y$, respectively. Initial particles with amplitudes up to $200\sigma_x$ and $240\sigma_y$ survived in the horizontal and vertical phase spaces, respectively. The horizontal and vertical RMS beam sizes in the long straight section were 34 μm and 31 μm, respectively. Here, $X(Y) = x(y)/\sqrt{\beta_{x(y)}}$ and $P_x(P_y) = [\alpha_{x(y)} + \beta_{x(y)}x'(y')\delta]/\sqrt{\beta_{x(y)}}$. In this expression, $\alpha_{x,y}$ and $\beta_{x,y}$ represent the Twiss parameters. x, y are the horizontal and vertical positions, and x', y' are the horizontal and vertical divergence angles, respectively. Figure 10c shows particle tracking in a longitudinal phase space that survives in the RF bucket of 4.1%. Here, $Z =$

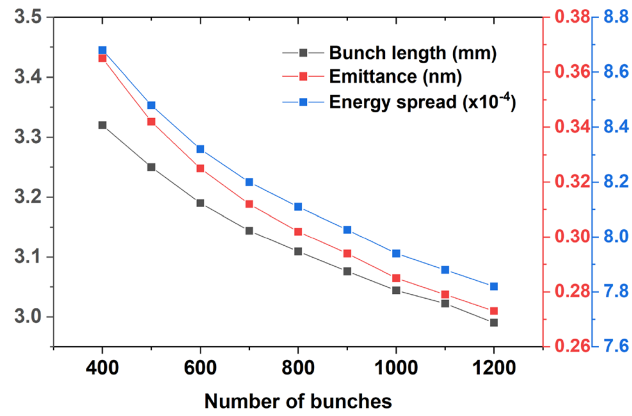

Fig. 6 (Color online) Bunch length (black), beam energy spread (red), and emittance (blue) versus number of bunches in the ring due to intrabeam scattering. Total beam current is 400 mA

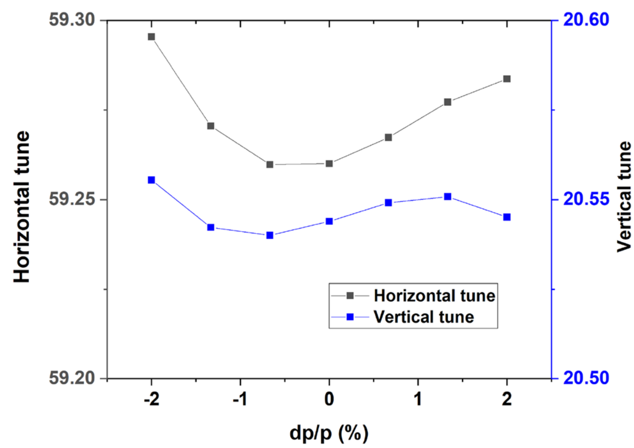

Fig. 7 (Color online) Horizontal and vertical tune shifts as a function of momentum deviation

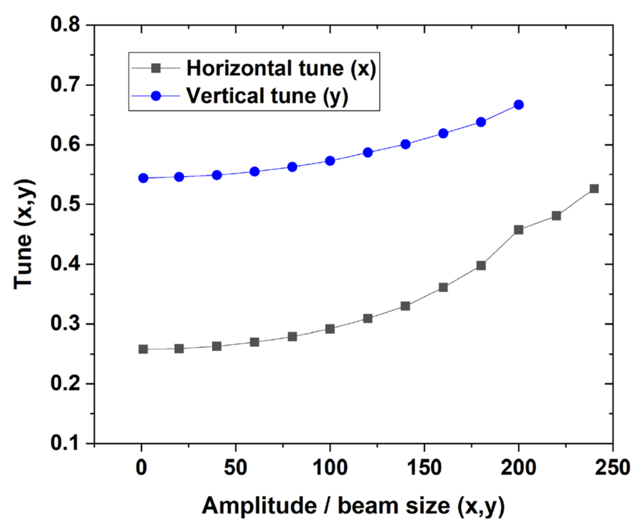

Fig. 8 Amplitude dependency in the horizontal and vertical tunes. The amplitude is normalized to the beam size in units of micrometers

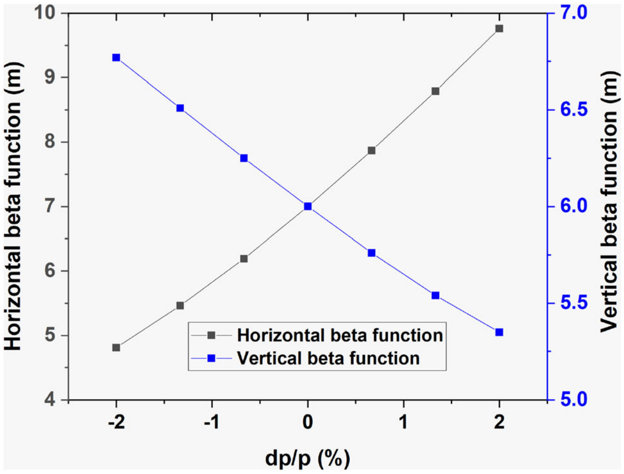

Fig. 9 (Color online) Horizontal and vertical beta functions as a function of momentum deviation

$z/\sqrt{\beta_z}$ and $P_z = (\alpha_z + \beta_z\delta)/\sqrt{\beta_z}$, where $\beta_z = \sigma_z/\sigma_\epsilon$. The momentum interval of the coordinates of the plotted particles is given by dP/P = 0.4%.

3 Dynamic aperture and error correction

It can be difficult to obtain an adequate dynamic aperture in the low-emittance lattice. Moreover, a wide dynamic aperture is required for efficient beam injection and beam lifetime. Strong sextupole magnets in the low-emittance lattice reduce the maximum amplitude of stable betatron motions and can affect beam lifetime. Thus, a thorough survey of the dynamic aperture is required to examine various machine errors and nonlinear effects of the sextupoles in the lattice. The motion of an off-momentum particle is also affected by the sextupoles. Thus, it is also necessary to extend the dynamic aperture by the COD correction. The lattice is also optimized to achieve a sufficient size of dynamic aperture.

The dynamic aperture was executed by six-dimensional particle tracking in SAD. We tracked the particles with the initial six-dimensional amplitudes in the designed lattice. If a particle survived for 1000 turns, it was assumed that its initial amplitude could continuously and stably maintain motion. The maximum initial amplitude was then defined to survive 1000 turns as the dynamic aperture. Because the particle amplitude was damped by synchrotron radiation, we assumed that 1000 turns were sufficient for stable particle motion. The particle tracking included both synchrotron motion and radiation damping. With these tracking studies, we selected an optimal tune with ν_x = 59.26 and ν_y = 20.54 for the lattice.

We considered the alignment errors of all magnets to examine the tolerance of the design lattice. The alignment errors of the magnets were determined after the misalignments in the ring were corrected. The values used were tolerable in most operational light sources. We combined the errors with the random horizontal and vertical alignment errors of 20 μm RMS in the quadrupoles, dipoles, and sextupoles. The errors were obtained from the Gaussian distribution with the RMS values truncated by 2.5σ in their distributions for tracking simulations. We employed 338 beam position monitors to monitor the horizontal and vertical orbits in the ring. The horizontal and vertical beam orbits were corrected using 338 horizontal and 338 vertical corrector magnets, respectively.

Figure 11 shows the dynamic apertures for the momentum deviations of ± 3% and 0% at the center of the long straight section. Figure 11a, b shows the dynamic apertures without machine errors and after COD correction with machine errors, respectively. The dynamic apertures were reduced by approximately 1 mm in both the horizontal and vertical directions for several random error seeds. This demonstrates that the lattice provided a sufficient aperture for horizontal off-axis beam injection in the ring. As the vertical physical aperture is primarily limited by in-vacuum undulators with gaps of approximately 3 mm, the vertical dynamic apertures in Fig. 11 were also acceptable. It is therefore shown that the dynamic apertures agree with the phase-space tracking results in Fig. 10.

Misalignment errors induce optical distortions and enhance the effects of resonances that reduce dynamic aperture. Beta-function distortions result in a larger beam size and may increase these effects. Large orbit distortions result in a reduction of the dynamic aperture because a particle is more significantly affected by nonlinear sextupole fields. Figure 12 shows distortions of the beta function (top), dispersion function (middle), and COD (bottom) due to machine errors. Figure 13 shows the beta function, dispersion function, and COD due to machine errors after COD correction. The results show that the beta function and dispersion function were well restored. Here, blue and red denote the horizontal and vertical directions, respectively. The horizontal and vertical orbits were well corrected within 50 μm. The strength of the corrector magnets was less than 0.1 mrad.

4 Beam injection

This section presents the injection scheme for full-energy injection into the ring. Figure 14 shows the horizontal space at the injection point. The injected beam was located 17.5 mm from the reference stored beam orbit. The injected beam oscillated with an amplitude of 12.5 mm around the stored beam in the ring.

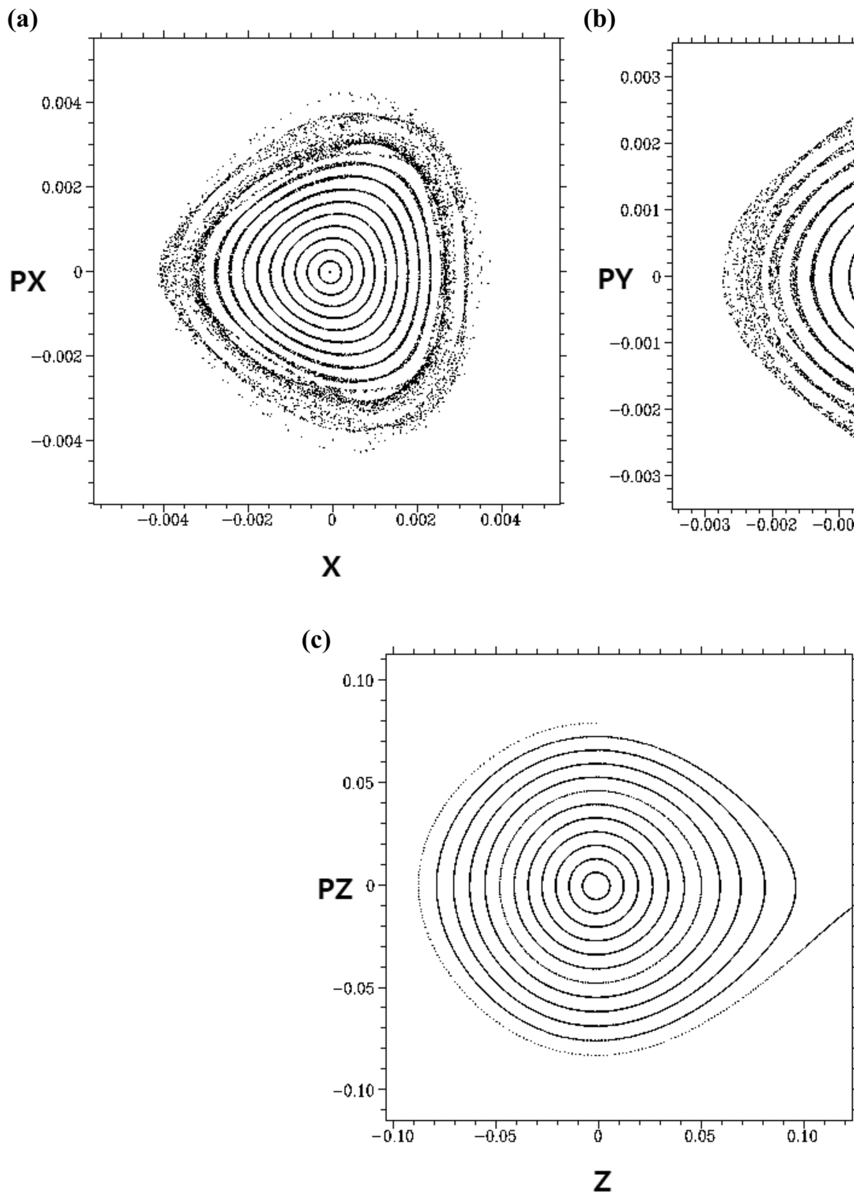

Fig. 10 Particle tracking in the **a** horizontal, **b** vertical, and **c** longitudinal phase spaces. The number of turns was set at 1000. The initial particles with horizontal amplitudes up to $200\sigma_x$ and $240\sigma_y$ survive in the horizontal and vertical phase spaces, respectively. **c** Particles in the RF bucket of 4.1% survive in the longitudinal phase space

Figure 15 shows the beta function, bump height, and bump kick angle in the injection section. The length and magnetic field of each kicker magnet were 0.6 m and 0.196 T, respectively. The distance between the first and second kickers was 0.7 m, and the distance between the two centered kickers was 1.4 m. This shows that the kick angle to obtain a bump height of 12 mm was given by − 9.23 mrad. The off-axis amplitude of the injected beam at the injection point was given by $6\sigma_{\mathrm{ix}} + t_{\mathrm{sep}} + 6\sigma_{\mathrm{sx}} =$ 5.5 mm, where σ_{ix}, t_{sep}, and σ_{sx} are the RMS beam size of the injected beam, effective thickness of the septum wall, and RMS beam size of the stored beam, respectively. The injection point had a maximum horizontal beta function in the ring. The dynamic aperture at the injection point should have been 5.5 mm. If the orbit distortion was 0.5 mm, the required dynamic aperture at the injection point would become 6 mm. The duration of the injection bump would correspond to one turn.

We performed six-dimensional multi-particle tracking for beam injection using SAD. Figure 16 shows the horizontal beam distributions in phase space for the injected beam for six turns after the injection. The beams injected into the ring were accumulated in the injection design scheme. Particle losses after the beam injection were

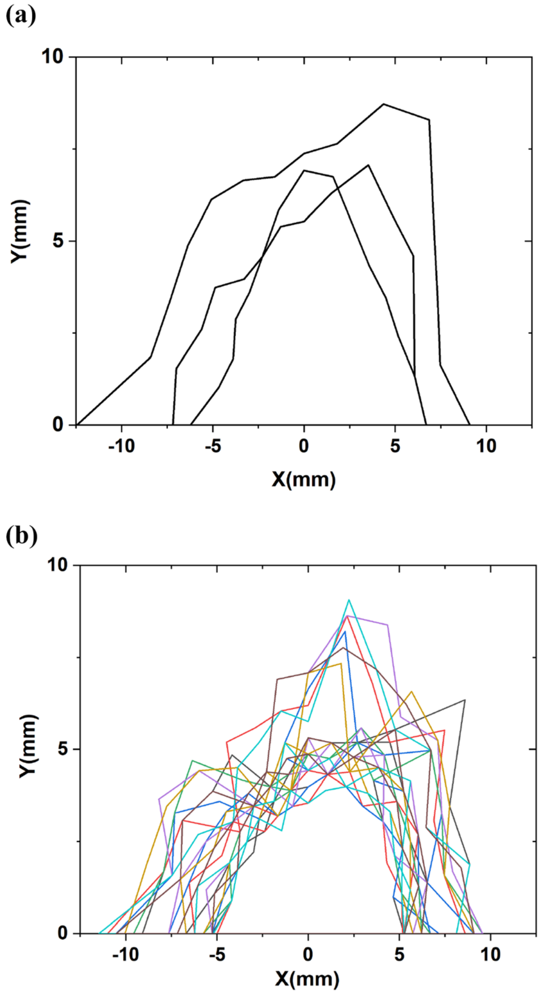

Fig. 11 (Color online) **a**, **b** The dynamic apertures without machine errors, and after COD correction and machine errors, respectively. Particles with several random error seeds are used in **b**

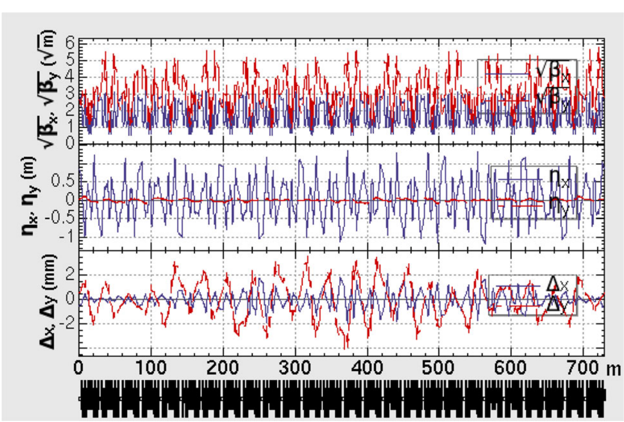

Fig. 12 (Color online) Beta functions (upper), dispersion functions (middle), and COD (lower) due to machine errors. Red and blue lines denote horizontal and vertical directions, respectively

shown to be zero. The beam orbits in both the horizontal and vertical directions were observed at each turn after the

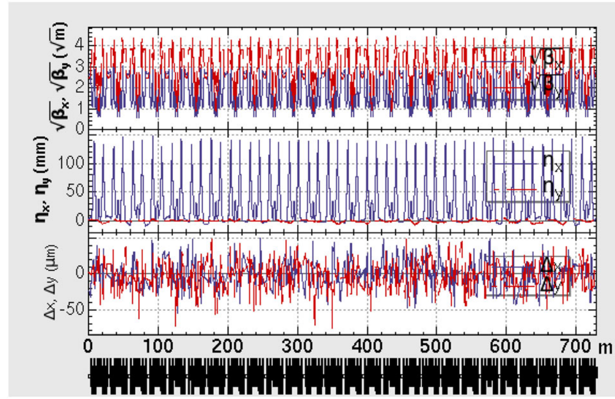

Fig. 13 (Color online) Beta functions (upper), dispersion functions (middle), and CODs (lower) after COD correction when machine errors are included. Red and blue lines denote horizontal and vertical directions, respectively

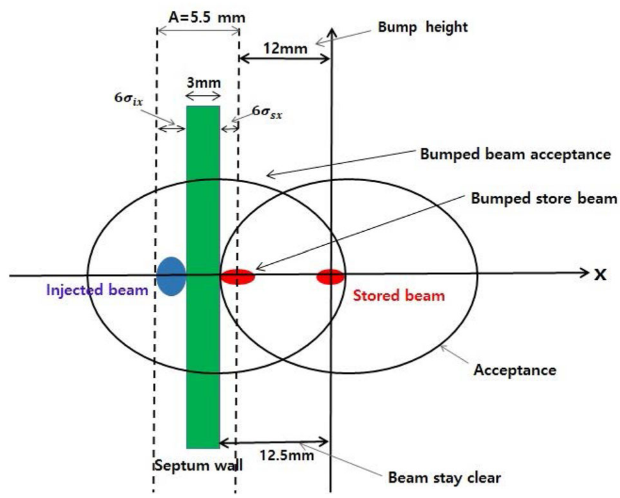

Fig. 14 (Color online) Horizontal space in the injection scheme

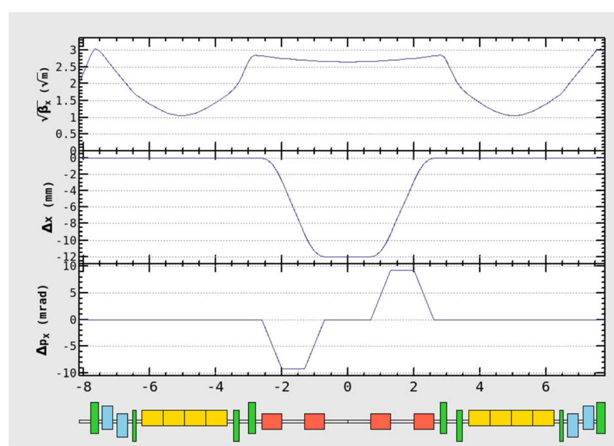

Fig. 15 (Color online) Beta functions, bump height, and bump kick angle in the injection. Four kicker magnets with length 0.6 m are shown in red

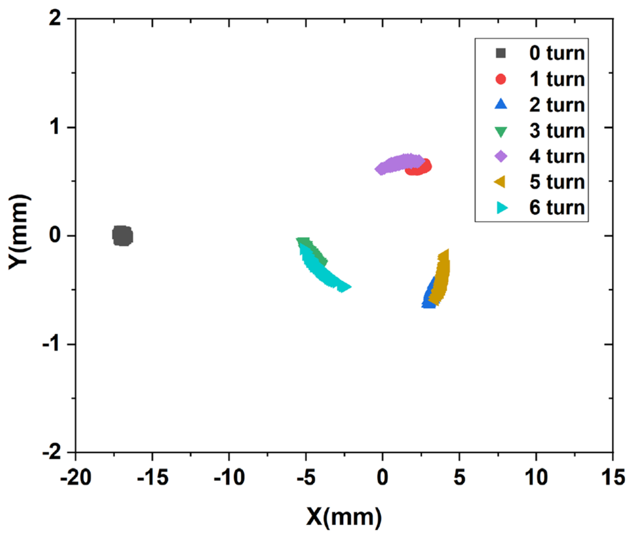

Fig. 16 (Color online) Horizontal beam distributions for five turns after the beam injection

beam injection. Figure 17 shows the horizontal and vertical beam orbits 1300 turns after the beam injection. The injected beam showed that the oscillation in the horizontal direction dampened rapidly within 60 turns. This indicated that the traditional injection scheme could be applied for

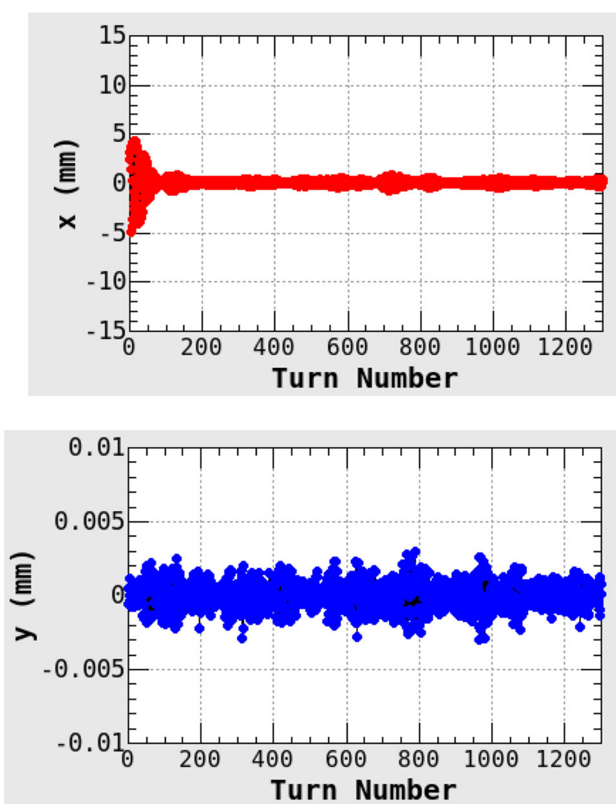

Fig. 17 (Color online) **a** Horizontal and **b** vertical beam positions as functions of the number of turns after beam injection

beam accumulation. Thus, the obtained dynamic aperture was also acceptable from a beam dynamics perspective.

5 Conclusion

We investigated lattice design and beam dynamics in a low-emittance ring with intermediate circumference and beam energy. An HMBA lattice for a 4 GeV ring was designed to produce high-brilliance synchrotron radiation for hard X-ray users. A storage ring with a natural emittance of 168 pm and 26 long and 26 short straight sections was designed as a light source. The dynamic aperture at the injection point was larger than 5 mm after COD correction. The lattice provided a sufficient size of dynamic aperture when machine errors were included and after COD correction. Thus, our designed ring showed optimized HMBA parameters for intermediate light sources in a 729.3 m ring. This study may provide a preliminary lattice design for future domestic storage rings. The traditional injection scheme with four kicker magnets can be applied to this design, and the Touschek lifetime may also be acceptable for the top-up injection and third harmonic cavity.

References

1. *Small Emittance Light Source Workshop*, Lund (2004)
2. M. Boege, Achieving sub-micron stability in light sources, in *Proceedings of 9th European Particle Accelerator Conference*, Lucern, 5–9 July, p. 211 (2004)
3. M. Abliz, M. Jaski, A. Xiao et al., A concept for canceling the leakage field inside the stored beam chamber of a septum magnet. Nucl. Instrum. Methods Phys. Res. A **886**, 7–12 (2018). https://doi.org/10.1016/j.nima.2017.11.090
4. M. Borland, Y. Sun, V. Sajaev, et al., Lower emittance lattice for the advanced photon source upgrade using reverse bending magnets, in *Proceedings of the North American Particle Accelerator Conference (NAPAC2016)*, Chicago, USA, pp. 877–880, 9–14 Oct (2016)
5. A. Streun, A. Wrulich, Compact low emittance light sources based on longitudinal gradient bending magnets. Nucl. Instrum. Methods Phys. Res. A **770**, 98–112 (2015). https://doi.org/10.1016/j.nima.2014.10.002
6. C. Steier, A. Allézy, A. Anders et al., Status of the conceptual design of ALS-U, in *Proceedings of IPAC2017*, Copenhagen, Denmark, 14–19 May, pp. 2824–2826 (2017)
7. B. Riemann, A. Streun, Low emittance lattice design from first principles: reverse bending and longitudinal gradient bends. Phys. Rev. ST Accel. Beams **22**, 021601 (2019). https://doi.org/10.1103/PhysRevAccelBeams.22.021601
8. D. Einfeld, M. Plesko, J. Schaper, First multi-bend achromat lattice consideration. J. Synchrotron Radiat. **21**, 856–861 (2014). https://doi.org/10.1107/S160057751401193X
9. Z. Dai, G. Liu and N. Huang, The SSRF storage ring magnet lattice design, in *Proceedings of Second Asian Particle Accelerator Conference*, Beijing, Sep. 369 Beijing 17–21 Sep (2001)

10. R. Nagaoka, A.F. Wrulich, Emittance minimisation with longitudinal dipole field variation. Nucl. Instrum. Methods Phys. Res. Sect. A **575**, 292–304 (2007).https://doi.org/10.1016/j.nima.2007.02.086
11. Y. Jiao, G. Xu, X.H. Cui et al., The HEPS project. J. Synchrotron Radiat. **25**, 1611–1618 (2018). https://doi.org/10.1107/S1600577518012110
12. W. Decking, K. Balewski. Optimization of low emittance lattices for PETRA III, in *Proceedings of the 9th European Particle Accelerator Conference*, Lucerne, 5–9 July, pp. 1225–1228 (2004)
13. A. Streun, Status of SLS lattice design, *Workshop on Nonlinear Dynamics in Particle Accelerators*, Arcidosso, Italy, 190, 4–9 Sept (1994)
14. Sirius. http://lnls.cnpem.br/
15. MAX-IV Detailed Design Report. https://www.maxiv.lu.se/accelerators-beamlines/accelerator-documentation/max-iv-ddr
16. ESRF-EBS. https://www.esrf.eu/about/upgrade (2018)
17. APS upgrade. https://www.aps.anl.gov/APS-Upgrade (2019)
18. http://acc-physics.kek.jp/SAD/